International Journal of Coal Geology 228 (2020) 103553

Contents lists available at ScienceDirect

International Journal of Coal Geology

journal homepage: www.elsevier.com/locate/coal

Evaluation and modeling of water vapor sorption and transport in nanoporous shale

Guijie Sang, Shimin Liu*, Derek Elsworth, Yun Yang, Long Fan

Department of Energy and Mineral Engineering, G³ Center and Energy Institute, The Pennsylvania State University, University Park, PA 16802, USA

ARTICLE INFO

Keywords:
Water Sorption
Surface Flow
Capillary Condensation
Diffusion Coefficient
Relative Humidity

ABSTRACT

Understanding vapor transport of water in nanoporous shale is challenging due to the coexistence of multiple water phases within a multi-mineral aggregate with complex multiscale pore architecture. We explore this response through dynamic vapor sorption experiments and modeling on two shale samples with differing fractions of hydrophilic clays and contrasting pore architecture. Measured diffusion coefficients of water vapor in the two shales are of the order of magnitude of 10^{-12} - 10^{-10} m^2/s, increasing with relative humidity (R_h) except at high R_h during adsorption process. The drop in diffusivity at high R_h during adsorption results from the impeding effect of capillary-occluding air bubbles and flattening of the pore-entry menisci. We propose a model for water vapor transport accommodating surface flow of adsorbed water and viscous flow of capillary water – with active mechanisms operational in different pore size populations. Actual pore size distributions (PSDs) are characterized by low pressure nitrogen adsorption. Predictions from the proposed transport model, utilizing these measured PSDs, are consistent with the measured diffusion behavior during desorption, also replicating water uptake behavior across the full spectrum of $0 < R_h < 1$. Observations and modeling illustrate that phase type and pore size significantly influence water vapor sorption and transport behaviors. Storage of the adsorbed phase dominates the total water uptake at low R_h (< 0.6) while the condensed phase dominates at $R_h > 0.6$. Surface flow of the adsorbed phase contributes predominantly to the total flux over a wide range of R_h (< 0.96) while viscous flow of capillary water dominates only at very high R_h values (> 0.98). In terms of pore size effects, macropores (> 50 nm) contribute little to the total water adsorption but comprise more than of the 68% total water flux. Conversely, micropores (< 2 nm), contribute moderately to water adsorption (7%–40%) but insignificantly to the total flux. Intermediate-sized mesopores (2–50 nm) play an important role in both total water adsorption and transport over the entire range of R_h. Sensitivity analysis of temperature (30–90 °C) indicates that diffusion coefficient of water vapor can be enhanced at higher temperature due to a lower viscous resistance of water to flow.

1. Introduction

Water-based drilling then hydraulic fracturing (Curtis, 2002) in gas shale reservoirs force the complex hydrodynamic interaction of water vapor and gas in both matrix and the fracture system. During the shut-in period of the well, a significant fraction of the injected water is spontaneously imbibed into the shale formation. Imbibition is controlled by relative permeability, capillary pressure, gravity segregation and fracture conductivity (Holditch, 1979; Cheng, 2010; Pang et al., 2014; Fan et al., 2019). Early-time gas production rate is typically enhanced due to gas buildup during this soaking period. Subsequent long-term production is additionally significantly influenced by the impacts of water-shale interactions on gas transport behavior. Water sorption directly impacts gas sorption and transport behavior in shales, as apparent in static sorption measurements (Gasparik et al., 2014; Yuan et al., 2014; Sun et al., 2017; Sun et al., 2018; Li et al., 2018a; Li et al., 2018b). Therefore, understanding of water vapor sorption and transport behavior in nano-porous shale matrix plays an important role in determining gas storage and transport behaviors under fully or partial water saturations, thus providing clues to predict long-term gas production.

Water vapor adsorption and transport in nano-porous shale are very complex due to the hydrogen-bonded nature of water (Luzar and Chandler, 1996) and the interplay of serval factors including mineral type (Sposito et al., 1999), kerogen (Bousige et al., 2016), and multi-scale pore size distribution (Clarkson et al., 2013). Complex surface

* Corresponding Author.
E-mail address: szl3@psu.edu (S. Liu).

https://doi.org/10.1016/j.coal.2020.103553
Received 5 April 2020; Received in revised form 10 July 2020; Accepted 11 July 2020
Available online 18 July 2020

Nomenclature

R_h	relative humidity
p_{wv}	partial pressure of water vapor, kPa
p_{wv}^0	saturated pressure of water vapor, kPa
r_{c_ads}	critical pore radius for condensation, Å
r_{c_des}	critical pore radius for evaporation, Å
R_g	universal gas constant, 8.314 J·mol^{-1}·K^{-1}
T	temperature, K
V_{lm}	molar volume of liquid water, m^3·mol^{-1}
M_w	molar mass of water molecules, kg·mol^{-1}
ρ_l	density of liquid water, kg·m^{-3}
σ	surface tension, N·m^{-1}
θ_c	contact angle, °
l_s	thickness of water film, Å
Θ	molecular coverage layers, −
C_l	molar concentration of liquid water, mol·m^{-3}
N	Avogardro number, mol^{-1}
C	BET constant, −
$f(r)$	pore volume distribution, cm^3·g^{-1}·Å^{-1}
ε_l	condensed pores, cm^3·g^{-1}
ε_s	adsorbed pores, cm^3·g^{-1}
ε_t	total pore volume per unit mass of shale based on pore size distribution, cm^3·g^{-1}
r_{ca}	actual critical pore radius, Å
S_w	percentage of water uptake in pores (or saturation)
V_{H2O}	total volume of water uptake, cm^3
V_{pore}	total pore volume of shale samples, cm^3
m_{H2O}	total mass of water uptake, g
m_{Sam}	total mass of shale samples, g
$m_{w\%}$	mass of water uptake per unit mass of shale
$V_{p\%}$	pore volume per unit mass of shale, cm^3·g^{-1}
J_s	surface flux of adsorbed phase, mol·s^{-1}·m^{-2}
J_l	fluid flux of liquid phase, mol·s^{-1}·m^{-2}
J_t	total fluid flux, mol·s^{-1}·m^{-2}
μ_s	dynamic viscosity of adsorbed water, Pa·s
μ_l	dynamic viscosity of liquid water, Pa·s
K_s	intrinsic permeability of pores with adsorbed water, Å^2
K_l	intrinsic permeability of pores with liquid water, Å^2
τ_s	tortuosity for the surface flow of adsorbed phase
τ_l	tortuosity for the viscous flow of liquid phase
C_{wv}	molar concentration of water vapor, mol·m^{-3}
C_s	molar concentration of adsorbed water, mol·m^{-3}
C_t	total molar concentration of water adsorption, mol·m^{-3}
n_{H2O}	moles of substance, mol
P_c	capillary suction, kPa
P_g	total gas (including water vapor) pressure, kPa
P_l	pressure of liquid water, kPa
D_{app}	apparent diffusion coefficient, m^2·s^{-1}
ρ_{bullk}	bulk density of shale sample, g·cm^{-3}
t	adsorption time, s
M_t	normalized mass adsorbed at time t, g·g^{-1}
M_∞	normalized mass adsorbed at thermodynamic equilibrium, g·g^{-1}
D_m	measured diffusion coefficient, m^2·s^{-1}
d	thickness of thin-section sample, m

Subscripts

wv	water vapor phase
s	adsorption phase
l	liquid phase
ads	adsorption process
des	desorption process

chemistry and pore structure determine water vapor sorption behavior (Thommes et al., 2013; Seemann et al., 2017; Tang et al., 2017; Sang et al., 2019; Yoro et al., 2019; Zhuravlev and Porokhnov, 2019). This involves a dominant mono−/multilayer adsorption at low relative pressure transitioning to dominant capillary condensation at high relative pressure (Gregg et al., 1982; Do, 1998). Thus, water vapor transport in nano-porous shales variously involves at least three different flow mechanisms over the spectrum of specific relative pressures of the water vapor, i.e. bulk diffusion of the vapor phase, surface diffusion of the adsorbed phase and flow of the capillary condensate (Choi et al., 2001; Sirghi, 2012). Knudsen diffusive flow plays an important role in bulk diffusion of the gas phase in the nanopores of the shale matrix (Javadpour et al., 2007; Sang et al., 2016) due to the dominance of collisions between molecules of adsorbate and the nanopore walls of the adsorbent. Compared to bulk flow of the gaseous phase, however, the surface flow of the adsorbed phase can be a significant fraction of the total mass flow in a porous medium (Schneider and Smith, 1968; Butt and Reed Jr, 1971; Sirghi, 2012). In addition, for condensable gases such as water vapor, capillary condensation at high relative pressures is another factor controlling the transport mechanisms (Rhim and Hwang, 1975; Lee and Hwang, 1986). In summary, a physics-based understanding of surface diffusion mechanisms and the role of capillary liquid water are essential in defining modes of water vapor transport in nano-porous shales.

Surface diffusion phenomena are commonly interpreted using site hopping (Okazaki et al., 1981) or hydrodynamic (Flood et al., 1952; Gilliland et al., 1958) models. The hopping model assumes that gas molecules hop randomly from site to site on the absorbent surface while the hydrodynamic model considers adsorbate as a liquid film which slides along the absorbent surface as driven by a pressure gradient. Both the hopping and hydrodynamic models have been applied to illuminate the underlying mechanisms driving the surface flow of the adsorbed phase and flow of the capillary condensate (Rowell et al., 1971; Rhim and Hwang, 1975; Tamon et al., 1981; Do, 1996; Chen and Yang, 1998). Typically, the diffusivity of condensable vapors in microporous or mesoporous media increases with an increase in partial pressure of the condensable vapor before declining at high partial pressures (Lee and Hwang, 1986). The initial increase of diffusivity with partial pressure is mainly due to the enhanced surface concentration (Do and Do, 2001). The decrease in diffusivity at high partial pressures could be attributed to either the occlusion of narrow pores induced by capillary condensation (Uhlhorn et al., 1992; Yoshimoto et al., 2017) or due to the reduction in capillary forces due to the flattening of the menisci at the pore-mouths (Lee and Hwang, 1986; Jaguste and Bhatia, 1995). Therefore, understanding of the role of surface diffusion and flow of condensed liquid water is the key in understanding water vapor transport in nano-porous shales. Still unclear, however, remains how the diffusivity of water vapor evolves with partial pressures in such nano-porous media due to the complex sorption mechanisms and the heterogeneity of the pore architecture.

This study probes mechanisms controlling water vapor transport in nanoporous shales through constrained experiments and analysis. Dynamic water vapor sorption experiments are conducted on thin sections of shale to characterize sorption isotherms with diffusion coefficients obtained from kinetic data. These observations support a modified water vapor transport model (Jaguste and Bhatia, 1995) that combines surface flow of adsorbed water and flow of capillary condensed water in the shale matrix. This accommodates the realistic pore size distribution obtained from physisorption measurements. Based on the experimental data and modeling results, the respective roles of surface diffusion of the adsorbed phase and of capillary flow of water are defined in contributing to the total water vapor flux over a full

spectrum of water vapor relative pressures.

2. Relative-pressure-dependent transport of water vapor

2.1. Ad/de-sorption equilibria

Mechanisms of evaporation and condensation in a mesoscale cylindrical capillary differ, resulting in hysteresis in the adsorption-desorption isotherm (Everett and Haynes, 1972; Gregg et al., 1982). The vapor-liquid equilibrium for capillary condensation during adsorption is governed by the Cohan equation (Cohan, 1938) of capillary thermodynamics as

$$\ln R_h = -\frac{\sigma V_{ml}}{r_{c\_ads} R_g T} \tag{1}$$

while that for capillary evaporation during desorption is represented by the Kelvin equation (Fisher et al., 1981; Israelachvili, 2011) as

$$\ln R_h = -\frac{2\sigma V_{ml} \cos\theta_c}{r_{c\_des} R_g T} \tag{2}$$

where $R_h = p_{wv}/p_{wv}{}^0$ is relative humidity; p_{wv} and $p_{wv}{}^0$ are partial and saturated pressure (kPa), respectively, of water vapor at a temperature T (K). r_{c_ads} and r_{c_des} are the critical pore radii during capillary condensation or evaporation, respectively; R_g, J·mol^{-1}·K^{-1}, is the universal gas constant; V_{ml}, m^3·mol^{-1}, is the molar volume of liquid water, depending on its molar mass M_w (kg·mol^{-1}) and density ρ_l (kg·m^{-3}) as: $V_{ml} = M_w/\rho_l$; σ (N·m^{-1}) is surface tension, and θ_c (°) is the contact angle. Here, r_{c_ads} represents the pore radius at which the thin films on opposing walls connect to form a liquid bridge during condensation and r_{c_des} represents the pore radius at which the capillary bridge starts to be ruptured during evaporation.

Assuming that the adsorbed layer has a liquid-like density, the film thickness (l_s) can be expressed as (Jaguste and Bhatia, 1995)

$$l_s = \frac{\Theta}{a_m N C_l} \tag{3}$$

where N is the Avogardro number, a_m is the molecular area of water and C_l is the molar concentration of liquid water. Θ is the number of molecular coverage layers for multiple adsorption, determined from BET theory as

$$\Theta = \frac{CR_h}{(1 - R_h)(1 - R_h + CR_h)} \tag{4}$$

where C is the BET constant related to interaction strength between water molecules and the solid surface of the shale.

The extent of pores filled with condensed water, defined as a "condensed pore volume" ε_l, can be determined from an integration of the volume of pores smaller than the actual critical pore radius where capillary condensation/evaporation occurs, defined as.

$$\varepsilon_l = \int_0^{r_{ca}} f(r)dr \tag{5}$$

where $f(r)$, cm^3·g^{-1}·Å^{-1}, is the pore size distribution, defined as the increment of pore volume $d\varepsilon$ over the size interval (r, $r + dr$), given as

$$f(r) = \frac{d\varepsilon}{dr} \tag{6}$$

The upper limit of the integral, r_{ca} in Eq. (5), is infinite and returns a total pore volume of ε_t. However, r_{ca} in Eq. (5) is actually a critical pore radius with different magnitudes for either capillary condensation or evaporation. During the adsorption process, due to pre-existing adsorbed layers that are present prior to the occurrence of capillary condensation, the actual critical pore radius is $r_{ca} = r_{c\_ads} + l_s$, where l_s is the thickness of these pre-existing adsorbed layers. During desorption, the actual critical pore radius is $r_{ca} = r_{c\_des}$, defining the criterion for evaporation. At the same relative humidity, the actual critical pore radius for capillary condensation is smaller than that for evaporation, causing the hysteresis between adsorption and desorption isotherms (Everett and Haynes, 1972; Gregg et al., 1982).

Assuming that pores may be represented as cylindrical capillaries, the extent of the adsorbed phase in vapor-filled pores, excluding the condensed pores, is given by:

$$\varepsilon_s = l_s \int_{r_{ca}}^{\infty} (2/r) f(r)dr \tag{7}$$

By assuming that the adsorbed phase is the same density as the liquid phase (ρ_{wl}), the total extent of water uptake S_w, also referred to as the degree of saturation, is defined as the total volume of pores occupied by water (including both adsorbed phase and condensed liquid phase) relative to the total pore volume at a specific relative humidity. S_w is defined as

$$S_w = \frac{V_{H2O}}{V_{pore}} = \frac{m_{H2O}/\rho_{wl}}{V_{pore}} = \frac{m_{H2O}/m_{Sam}/\rho_{wl}}{V_{pore}/m_{Sam}} = \frac{m_{w\%}/\rho_{wl}}{V_{p\%}} \tag{8}$$

where V_{H2O} and V_{pore} are the volume of water uptake and total pore volume, respectively; m_{H2O} and m_{Sam} are the mass of water uptake and of the shale sample, respectively. $m_{w\%} = m_{H2O}/m_{Sam}$ is the mass of water uptake per unit mass of shale sample as a measurable quantity from a dynamic water vapor sorption experiment. $V_{p\%} = V_{pore}/m_{Sam}$ is the pore volume per unit mass of the shale sample, which can also be directly obtained from low pressure nitrogen adsorption. By definition, and based on Eqs. (5) and (7), the degree of saturation can be also expressed as $S_w = (\varepsilon_l + \varepsilon_s)/\varepsilon_t$. These component quantities of Eq. (8) may be directly measured, as detailed in Section 4.3.

2.2. Surface flow in adsorbed phase

According to the hydrodynamic model proposed by Flood and coworkers (Flood et al., 1952; Flood and Huber, 1955), flow of the adsorbed phase can be treated as liquid flow with the adsorbed molecular layers sliding across the surface of the adsorbent. The driving force for the surface flow of the adsorbed phase is the gradient of hydrostatic stress intensity ∇P_s (Pa·m^{-1}). The surface flux, J_s (mol·s^{-1}·m^{-2}), can be expressed as (Jaguste and Bhatia, 1995)

$$J_s = -\frac{K_s}{\mu_s} C_s \nabla P_s \tag{9}$$

where C_s, mol·m^{-3}, is the molar concentration of the adsorbed phase. Assuming that the adsorbed and condensed phases have the same density, C_s is equal to the molar concentration of condensed liquid water ($C_s = C_l = 1/V_{ml} = \rho_l/M_w$).

In Eq. (9), μ_s, Pa·s, is the dynamic viscosity of the adsorbed water. The viscosity in the vicinity of a pore wall is typically larger than that of bulk water due to the interaction between the pore wall and the confined fluid film (Raviv et al., 2001). Wu et al. (2017) derived an empirical relationship between the confined viscosity μ_s, of adsorbed water in this case, and fluid wettability based on experiments and molecular dynamics simulations from the literature. μ_s can be expressed as a function of contact angle θ_c and dynamic viscosity of liquid bulk water μ_l, given as (Wu et al., 2017)

$$\mu_s = (-0.018\theta_c + 3.25)\mu_l \tag{10}$$

At a particular relative humidity, R_h, the pores within a porous solid can be divided into three types depending on their occupation by water phases: voids filled with condensed liquid water (radii smaller than r_{ca}), voids occupied by water vapor (radii larger than r_{ca}), and voids occupied by adsorbed water (radii larger than r_{ca}). K_s in Eq. (9) is the effective permeability of a porous solid associated with the adsorbed phase. K_s excludes the voids occupied by vapor and liquid phases. Assuming that pores are cylindrical, K_s defined as

$$K_s = \frac{1}{8\tau_s}\int_{r_{ca}}^{\infty}[r^2-(r-l_s)^2]f(r)dr = \frac{1}{8\tau_s}\int_{r_{ca}}^{\infty}(2rl_s-l_s^2)f(r)dr \quad (11)$$

where τ_s is the tortuosity of the surface flow of the adsorbed phase in vapor-filled pores.

Flood (1961) assumes local thermodynamic equilibrium between the adsorbed and vapor phases, and therefore recovers the relation

$$\frac{dp_{wv}}{dP_s} = \frac{C_{wv}}{C_s} \quad (12)$$

where C_{wv}, mol·m^{-3}, is the molar concentration of water vapor in the gas phase. Combining Eqs. (9) and (12) together with the ideal gas law ($P_{wv} = C_{wv}\cdot R_g\cdot T$) yields the surface flux J_s as

$$J_s = -\frac{K_s C_s^2 R_g T}{\mu_s P_{wv}}\nabla p_{wv} \quad (13)$$

2.3. Viscous flow of capillary condensate

The viscous flow of capillary condensate, J_l, can be described as

$$J_l = -\frac{K_l}{\mu_l}C_l\nabla P_l \quad (14)$$

where ∇P_l is the pressure gradient of condensed water. K_l is the intrinsic permeability of the liquid phase within the pores, defined as

$$K_l = \frac{1}{8\tau_l}\int_0^{r_{ca}} r^2 f(r)dr \quad (15)$$

where τ_l is the tortuosity for the flow of capillary condensate in liquid-filled pores. r_{ca} is the actual critical pore radius, as is described in Section 2.1, which differs between adsorption or desorption, even at the same relative humidity and controls the hysteretic response.

As water vapor pressure increases, capillary condensation progressively occurs from smaller to larger pores. Due to the interfacial tension at the liquid-air interface, the pressure in the vapor phase P_g is larger than that in the condensed liquid phase P_l. Thus the gradient of capillary suction ∇P_c acts as a net force driving the displacement of capillary condensate. According to the Young–Laplace equation, capillary suction is given as

$$P_c = P_g - P_l = \frac{2\sigma\cos\theta_c}{r_c} \quad (16)$$

Combining Eqs. (2) and (16) yields

$$\ln\frac{P_{wv}}{p_{wv}^0} = -\frac{V_{ml}(P_g-P_l)}{R_g T} \quad (17)$$

where V_{ml} is the molar volume of the condensed liquid water as described previously ($V_{ml} = 1/C_l$). Thus, the pressure gradient of condensed water ∇P_l for the case of constant vapor phase pressure P_g is recovered from Eq. (17), as

$$\nabla P_l = \frac{R_g T C_l}{p_{wv}}\nabla p_{wv} \quad (18)$$

Combining Eqs. (14) and (18) yields

$$J_l = -\frac{K_l R_g T C_l^2}{\mu_l p_{wv}}\nabla p_{wv} \quad (19)$$

When a capillary fills with condensate, a further increase in relative humidity will cause the flattening of the meniscus at the pore-mouth (Rhim and Hwang, 1975; Lee and Hwang, 1986; Jaguste and Bhatia, 1995) and hence reduce capillary suction, consistent with Eq. (16). This leads to a decrease in the driving force for transport by capillary condensation. After the entire pore is filled by bulk condensation, the gradient of the total gas pressure acts as a driving force for condensate flow obeying the Hagen-Poiseuille equation (Rhim and Hwang, 1975; Lee and Hwang, 1986; Jaguste and Bhatia, 1995; Choi et al., 2001). For different relative humidities for an open system, the total gas pressure is constant in space, thus gradient $\nabla P_g = 0$. Therefore, the flow rate in the condensed pores progressively approaches zero with the flattening of the menisci at the pore-mouths. Lee and Hwang (1986) considered a cylindrical pore as being fully-saturated when the thickness (l_s) of the adsorbed phase is equal to or greater than the pore radius. Based on this concept, Eq. (15) can be rewritten as

$$K_l = \frac{1}{8\tau_l}\int_{l_s}^{r_{ca}} r^2 f(r)dr \quad (20)$$

where the lower integration limit is the film thickness (l_s) of adsorbed water. Lacking a meniscus at the pore-mouth, pores smaller than the thickness of the adsorbed phase, no longer contribute to the total flux.

2.4. Apparent diffusion coefficient

Vapor phase flow in mesoporous materials is negligible when compared to the dominant contributions of surface flow and flow of capillary condensate (Schneider and Smith, 1968; Butt and Reed Jr, 1971; Choi et al., 2001; Sirghi, 2012). The total flux (J_t) of water vapor in shale pores consists of surface flow in the adsorbed phase (J_s) and viscous flow of the condensed liquid (J_l), expressed as

$$J_t = J_s + J_l \quad (21)$$

According to Fick's law, the total mass flux can also be expressed by the apparent diffusion coefficient D_{app} as

$$J_t = -D_{app}\nabla C_t \quad (22)$$

where C_t is the total molar concentration of water adsorbed at a particular relative humidity, R_h. Combining Eqs. (13), (19), (21) and (22) yields the apparent diffusion coefficient as

$$D_{app} = \frac{R_g T}{p_{wv}}\left(\frac{K_s C_s^2}{\mu_s}+\frac{K_l C_l^2}{\mu_l}\right)\left(\frac{dp_{wv}}{dC_t}\right)_{P_{wv}} \quad (23)$$

where the effective permeability of a porous solid associated with the adsorbed phase (K_s), and intrinsic permeability associated with the condensed liquid phase (K_l) are given by Eqs. (11) and (20), respectively. The total molar concentration of water adsorption can be expressed as

$$C_t = \frac{n_{H2O}}{V_{pore}} = \frac{m_{H2O}}{M_w}\frac{1}{V_{pore}} = \frac{1}{M_w}\frac{m_{H2O}}{m_{Sam}}\frac{m_{sam}}{V_{pore}} = \frac{\rho_{bulk}}{\varepsilon_t M_w}m_{w\%} \quad (24)$$

where V_{pore} is the total pore volume and can be expressed as the ratio of bulk density (ρ_{bullk}) to total pore volume per unit mass of samples (ε_t) as: $V_{pore} = \rho_{bullk}/\varepsilon_t$; n_{H2O} and m_{H2O} represent water uptake at a particular relative humidity defined as number of moles and total mass, respectively. As defined previously, m_{Sam} is the mass of the shale sample and $m_{w\%} = m_{H2O}/m_{Sam}$ is the mass of water uptake per unit mass of shale sample, directly measured experimentally. Thus, the second bracketed term in Eq. (23) can be determined from the slope ($dm_{w\%}/dR_h$) of the water adsorption isotherm as

$$\left(\frac{dp_{wv}}{dC_t}\right)_{P_{wv}} = \frac{p_{wv}^0 dR_h}{dC_t} = \frac{p_{wv}^0 M_w \varepsilon_t}{\rho_{bulk}}\frac{1}{(dm_{w\%}/dR_h)_{P_{wv}}} \quad (25)$$

Combining Eqs. (23) and (25) yields the final form of the apparent diffusion coefficient as

$$D_{app} = \frac{R_g T M_w \varepsilon_t}{\rho_{bulk} R_h}\left(\frac{K_s C_s^2}{\mu_s}+\frac{K_l C_l^2}{\mu_l}\right)\frac{1}{(dm_{w\%}/dR_h)_{P_{wv}}} \quad (26)$$

In this model, all the parameters are either constants or may be directly measured experimentally, except for the tortuosity factors τ_l in Eq. (11) and τ_s in (20) - which are intrinsically difficult to determine for realistically heterogeneous and complex nano-porous shales. The tortuosity factors may be approximated by the following empirical relationship (Jaguste and Bhatia, 1995).

$$\tau = \left(\frac{\varepsilon_t}{\varepsilon_l}\right)^n \tau^* \quad (27)$$

where n and τ^* are fitting parameters potentially recovered from model calibration. Eq. (27) suggests that the tortuosity factors for surface flow and flow of capillary condensation are influenced by condensed pore volume ε_l, which is determined by relative humidity and pore size distribution.

2.5. Assumptions and limitations

Modeling of sorption and transport behaviors in highly heterogeneous shale with multi-scale pore architecture and complex wetting characteristics is extremely challenging. This requires a series of simplifications and basic assumptions for the establishment of the model. Firstly, we adopted assumption from (Do and Do, 2001) that surface chemistry of the flat surface and the surface of the pore walls are similar so that the pore dimension is the only factor that makes adsorption in the pore different from that occurring on a flat surface. Note that in some recent studies (Seemann et al., 2017; Sang et al., 2019; Lahn et al., 2020), surface chemistry plays a more important role than pore structure at low relative humidity. Though water transport behavior is highly associated with pore structure, the surface-chemistry-controlled sorption behavior of water vapor in shales at low relative humidity may not be directly linked with the pore structure. Therefore, there exist some limitations when applying this model to describe the water vapor sorption behavior in nano-porous shales. Secondly, we assume that pores are in cylindrical shape with a homogeneous wettability. For organic-rich shales containing a large number of hydrophobic pores, one may need to quantitative distinguish these hydrophobic organic pores from hydrophilic inorganic pores (Zolfaghari et al., 2017a; Zolfaghari et al., 2017b) in order to apply this transport model. The model also assumes that there is no alteration of pore structure during sorption process. This assumption (no structural alterations) may be reasonable by the most recent work through a reproducibility test (Lahn et al., 2020). However, in shales containing high content of expansive smectite, swelling pressure may trigger irreversible alteration of the pore structure (Huang et al., 1986; Brattli and Broch, 1995) and hence fail the transport model. We want to point out that these assumptions are important to simplify the modeling process. If the assumption cannot be met, the model should be further modified to incorporate the mineral and pore structure information for the prediction of the water vapor sorption and diffusion behaviors.

3. Experimental observations

3.1. Sample collection and characterization

Two samples of lower Silurian Longmaxi shale are collected from the southern Sichuan Basin, China. The samples are pulverized and characterized by: X-ray diffraction (XRD) to define the mineralogical components, and for total organic carbon (TOC), vitrinite reflectance (R_o), and by low pressure N_2 adsorption to define the pore size distribution. Thin section samples for the two shales (dimension: ~0.6 mm × 10 mm × 10 mm) are prepared for water vapor sorption and diffusion experiments conducted using the dynamic vapor sorption (DVS) instrument. Diffusion coefficients for water vapor are measured for the two shale samples over a wide range of relative humidities, R_h, (0%–95%) using the water kinetic data obtained from the DVS instrument.

The weight percentage of minerals and TOC are summarized in Table 1. The two shales show relatively high contents of quartz (27.3%, 49.8%), moderate TOC contents (2.1%, 2.7%) but with contrasting clay (67%, 11.8%) and calcite (2.3%, 35.7%) contents. The Nanchuan shale is of high clay content (67%) and contains small amounts of pyrite (1.3%), calcite (2.3%) and TOC (2.1%), while the Yibin shale is calcite rich (35.7%) but with low clay content (11.8%).

3.2. Low pressure N_2 adsorption

Low pressure N_2 adsorption experiments are performed on the powdered samples (#60-#80 mesh) using a Micromeritics ASAP 2020 instrument. Prior to the low pressure N_2 adsorption measurements, the two samples are degassed at 100 °C for approximately 10 h. The relative pressure for N_2 adsorption ranges from 0.009 to 0.994 (Fig. 1). The Brunauer–Emmett–Teller (BET) model is used for the estimation of the specific surface area (SSA) while BJH and DFT theory are used for the estimation of the total pore volume (PV) and pore size distribution (PSD), respectively. The interpretation of the N_2 sorption isotherms is discussed in previous studies (Gregg et al., 1982; Thommes, 2010; Rouquerol et al., 2013).

Results from low pressure N_2 adsorption are listed in Table 2. The Nanchuan shale shows a larger BET surface area (17.4 m^2/g) and pore volume (0.026 cm^3/g) for pore radii in the range from 1.7 to 300 nm relative to Yibin shale with BET surface area and pore volumes of 12.5 m^2/g and 0.019 cm^3/g, respectively. PSDs $f(r)$ for the two shale samples are also characterized by low pressure N_2 adsorption, using DFT theory, with results shown in Fig. 2. These fitted PSDs (red line) are ultimately incorporated into the transport model developed in Section 2 (Eqs. (5), (11), and (20)) to independently evaluate the apparent diffusion coefficients (Eq. (26)) for the two shale samples.

3.3. Water vapor uptake and diffusion measurements

3.3.1. DVS analysis and ad−/desorption isotherms

Water vapor sorption experiments are performed by dynamic vapor sorption (DVS) on the two thin-section (thickness ~ 0.6 mm) samples of shale. The schematic representation of the DVS setup is shown in Fig. 3. Dynamic changes in mass under different sample environments are measured by microbalance with a sensitivity of 0.1 μg ± 1%. Temperature is maintained constant as 30 °C with prescribed relative humidities (R_h) achieved by adjusting the respective flow rates of mixing wet and dry flow streams controlled by two mass flow controllers (MFCs). Further details of the experimental procedure are presented elsewhere (Seemann et al., 2017; Sang et al., 2019).

Fig. 4 shows the results of dynamic water vapor sorption on both Nanchuan and Yibin shales for a full wetting-drying cycle at 30 °C. Under initial quasi-dry conditions (~ 0% R_h) the residual water desorbs to reach an equilibrium state as identified where mass of the sample decreases to a final constant value – this is considered the mass for the true-dry state. Then water vapor ad/de-sorption isotherms are evaluated from observed changes in the equilibrium mass per unit mass relative to this true-dry state. Water vapor ads−/desorption isotherms are shown in Fig. 5 with both exhibiting a slight hysteresis during desorption. The sorption capacity of the Nanchuan shale is significantly higher than that for the Yibin shale - attributed to the higher clay content (Table 1) and higher mesopore volume in the Nanchuan shale (Table 2). The hydrophilic surfaces of clay minerals and increased pore volume provide a greater number of primary sites for water uptake in shale samples. The impacts of mineralogical composition and pore structure on water vapor adsorption are detailed elsewhere (Sang et al., 2019).

Table 1
Weight percent of mineralogical components and TOC of Nanchuan and Yibin shales.

Sample	Quartz, %	Clay minerals, %	Pyrite, %	Calcite, %	TOC, %	R_o, %
Nanchuan	27.3	67.0	1.3	2.3	2.1	3.2
Yibin	49.8	11.8	–	35.7	2.7	1.9

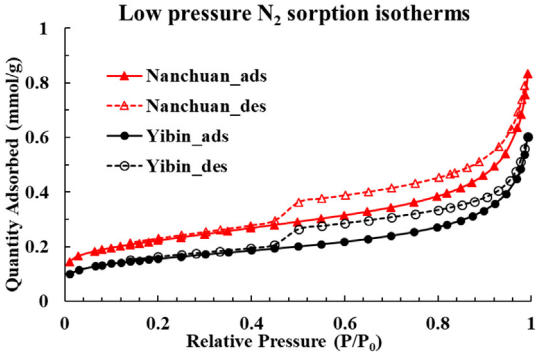

Fig. 1. Low pressure N_2 adsorption isotherms at 77 K.

Table 2
Pore structure characterization of Nanchuan and Yibin shale based on low pressure N_2 adsorption.

Sample	BET surface area, m^2/g	BJH pore volume ($v_{p\%}$), cm^3/g	Average pore size, Å
Nanchuan	17.4	0.026	63.0
Yibin	12.5	0.019	61.9

3.3.2. Estimation of diffusion coefficients

Water vapor transport into a thin slice shale sample (plane sheet) can be represented as linear diffusion in 1D from a surface at constant potential as (Crank, 1979)

$$\frac{M_t}{M_\infty} = 4\left(\frac{D_m t}{d^2}\right)^{1/2}\left\{\pi^{-\frac{1}{2}} + 2\sum_{n=1}^{\infty}(-1)^n \text{ierfc}\frac{nd}{2\sqrt{D_m t}}\right\} \quad (28)$$

where M_t and M_∞ are the masses of water uptake at time t and at thermodynamic equilibrium, respectively. D_m is diffusion coefficient and d is thickness of the slice sample. For early time, where $M_t/M_\infty < 0.4$, the above summation may be simplified and approximated as

$$\frac{M_t}{M_\infty} = \frac{4}{d}\left(\frac{D_m t}{\pi}\right)^{1/2} \quad (29)$$

Fig. 6 shows an example of the kinetic data, M_t/M_∞ plotted relative to the parameter $t^{1/2}$/d ($s^{1/2}$/m), for Nanchuan shale at $R_h = 40\%$ and $T = 30$ °C. The early-time slope of M_t/M_∞ versus ($t^{1/2}$/d) enables the diffusion constant D_m to be estimated from Eq. (29). Thus, the diffusion

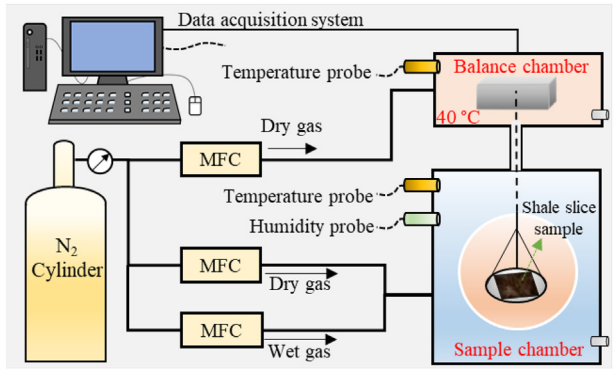

Fig. 3. Schematic representation of the DVS experimental setup. MFC represents mass flow controller.

coefficient at each prescribed relative humidity may be recovered from the kinetic data for as each sorption equilibration is approached. This procedure is repeated for all incremented then decremented relative humidities (Fig. 4) and for each shale.

4. Modeling results and discussion

4.1. Water vapor transport modeling

Basic material properties used in the experiments are listed in Table 3, among which only the bulk density of the shale is an assumed value (2.5 g·cm^{-3}). All other variables in this study are either calculated from basic model parameters or obtained through direct experimental measurement. The PSD was recovered from low pressure nitrogen adsorption (Fig. 2) with lower and upper cutoffs of 5 and 800 Å, respectively. The water vapor adsorption isotherm was directly measured by DVS as shown in Fig. 5. The three necessarily remaining fitting parameters were tortuosity factors τ_s^*, τ_l^* and n. Note that these three fitting parameters are the same for both adsorption and desorption.

The modeled water vapor diffusion coefficients for both Nanchuan and Yibin shales are shown in Fig. 7. The fitting parameters are $\tau_s^* = 16$, $\tau_l^* = 30$, $n = 0.5$ for Nanchuan shale and $\tau_s^* = 18$, $\tau_l^* = 30$, $n = 0.5$ for Yibin shale. Overall, the model satisfactorily represents the evolution of diffusion coefficient during the desorption process as illustrated by the congruence between the model (black dashed-line) with observations (black hollow circles) in Fig. 7. Using the same fitting parameters for the adsorption process, the modeled results also agree well with the experimental data for $R_h \leq 0.8$ but overestimates the

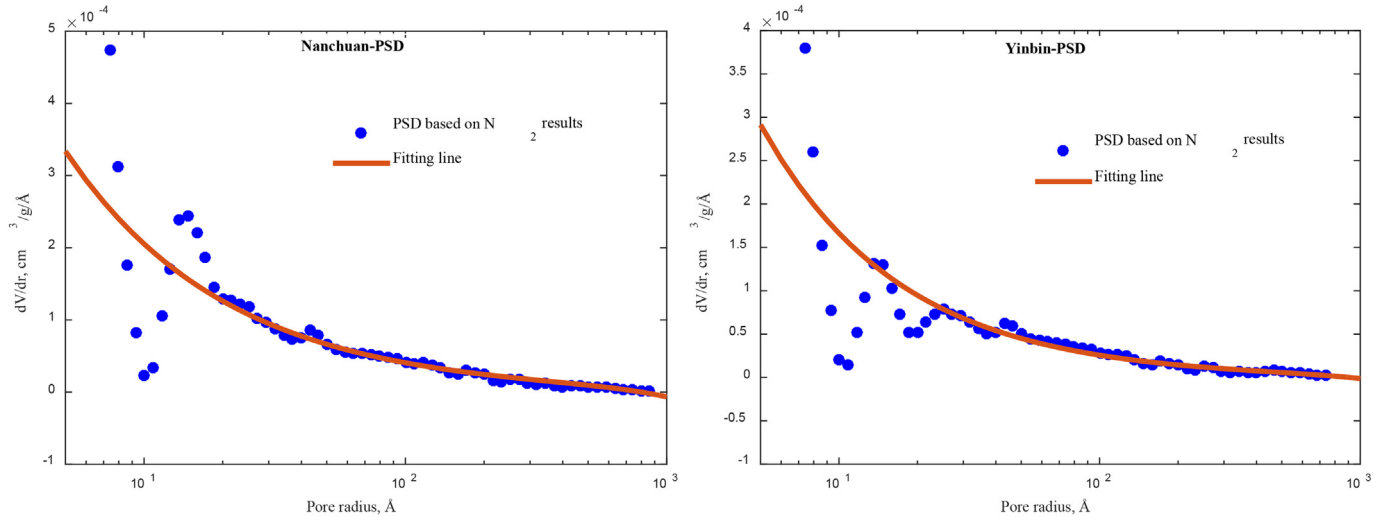

Fig. 2. Pore size distributions (PSD) and idealized curve fits of the two shales, based on DFT analysis.

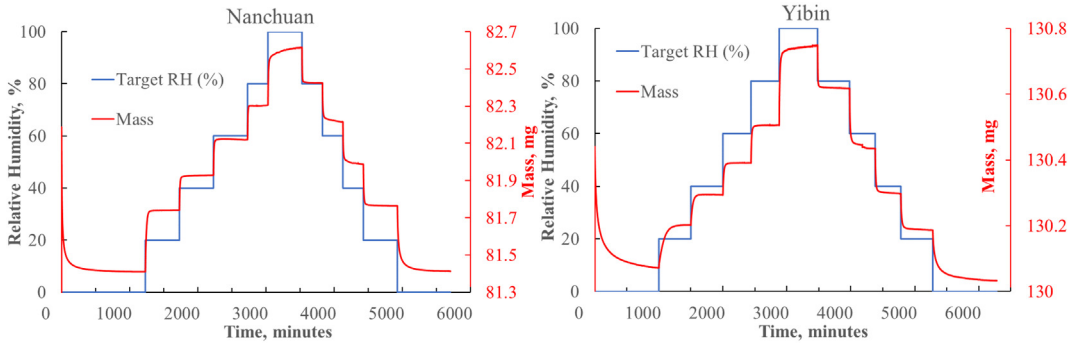

Fig. 4. Experimental results for dynamic water vapor sorption on Nanchuan (*left*) and Yibin (*right*) shales at 30 °C.

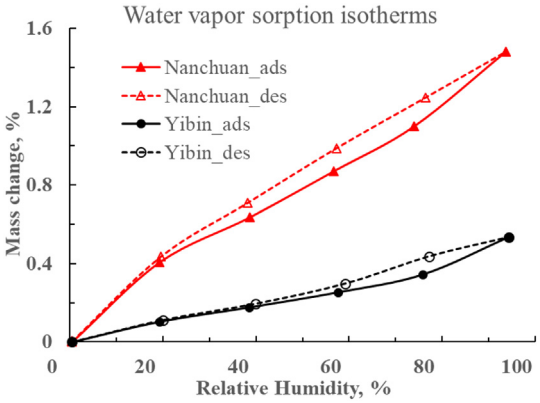

Fig. 5. Water vapor sorption isotherms for the two shales at 30 °C.

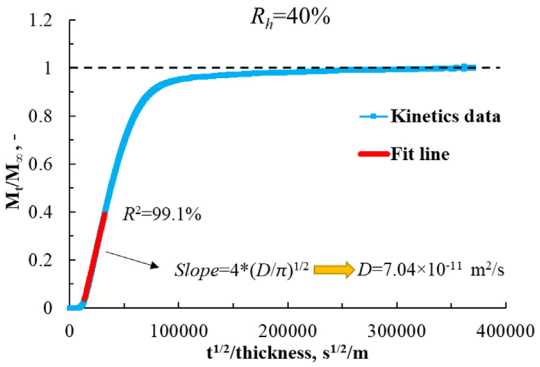

Fig. 6. Kinetic data for water vapor transport (diffusion) into Nanchuan shale at R_h = 40%, 30 °C.

diffusion coefficient for R_h > 0.8. The discrepancy between the adsorption and desorption could be attributed to pore morphology and pore network interconnectivity of shale (Cychosz et al., 2017). Details of water vapor transport mechanisms and posited reasons for this mismatch are discussed in the subsequent section. From Fig. 7, it is apparent that the modeled diffusion coefficient for desorption (black dash line) is slightly higher than that for adsorption (red solid line) – this may be due to hysteresis in ad−/de-sorption (Ravikovitch and Neimark, 2005; Naumov et al., 2007). For both shales, the diffusion coefficients measured at high R_h (~0.94) show a large difference during desorption relative to adsorption, as illustrated in Fig. 7. This can be explained by the different vapor transport mechanisms detailed in the following Section.

4.2. Discussion of water vapor transport mechanisms

There are several explanations for the observed drop in the diffusion

Table 3
Basic material properties and experimental parameters.

Parameter	Symbol	Value	Unit
Avogardro number	N	6.022×10^{23}	mol^{-1}
Molecular area of water	a_m	10.6	$Å^2$
Density of liquid water	ρ_l	0.996	$g{\cdot}cm^{-3}$
Molar mass of water	M_w	18.015	$g{\cdot}mol^{-1}$
Molar concentration of liquid water[a]	C_l	0.055	$mol{\cdot}cm^{-3}$
Surface tension	σ	0.0712	$N{\cdot}m^{-1}$
Temperature	T	303.15	K
Universal gas constant	R_g	8.314	$J{\cdot}mol^{-1}{\cdot}K^{-1}$
Dynamic viscosity of liquid water at 30 °C	μ_l	0.000798	Pa·s
Contact angle	θ_c	0	°
Bulk density of shale[b]	ρ_{bullk}	2.5	$g{\cdot}cm^{-3}$

[a] Molar concentration of liquid water is calculated based on the relation $C_l = \rho_l/M_w$.
[b] Bulk density of shale is an assumed value.

coefficient measured at high R_h during adsorption. First, based on the concept of equivalent bundles of cylindrical capillaries, Lee and Hwang (1986) extended a six-mode flow model (Rhim and Hwang, 1975) by considering the blocking effect of the adsorbed phase. The six-mode flow model (Rhim and Hwang, 1975; Lee and Hwang, 1986), as illustrated in Fig. 8, adequately reproduces a peak diffusivity at high relative pressure for a single capillary. At low relative pressures, bulk diffusion of vapor and surface diffusion of the adsorbed phase dominate the initial flow mode (F1). With an increase in relative pressure, the diffusivity rises as capillary condensate deposits then grows (flow modes F2, F3 & F4), before sharply decreasing as the capillary is fully-filled with condensate. The decrease in diffusivity at high relative pressure is due to the transition in the flow mode, transiting from capillary (force) dominated to one driven by the gradient of the total gas pressure (Rhim and Hwang, 1975; Lee and Hwang, 1986; Jaguste and Bhatia, 1995), as the capillary saturates. Note that surface flow of the adsorbed phase and viscous flow of capillary condensate may co-exist in different pores, although not within the same pore. Thus the relative contribution of these different transport modes is dependent on both the real pore size distribution and relative humidity.

Considering a real pore size distribution characterized by low pressure nitrogen adsorption, Jaguste and Bhatia (1995) attributed the occurrence of the peak permeability/diffusivity at high R_h values to a reduction in capillary force. The authors argued that a single capillary is much more permeable to the condensable component when condensate occurs. Once the capillary is filled with condensate (flow mode F3 in Fig. 8), however, any further increase in relative pressure will cause a flattening or loss of the meniscus at the pore-mouth (flow modes F4, F5 & F6 in Fig. 8). This would lead to a reduction in the capillary suction pressure and hence to a reduction in the driving force controlling the displacement of the capillary condensate. Nevertheless, our modeling results (detailed in the next section) show that the contribution of

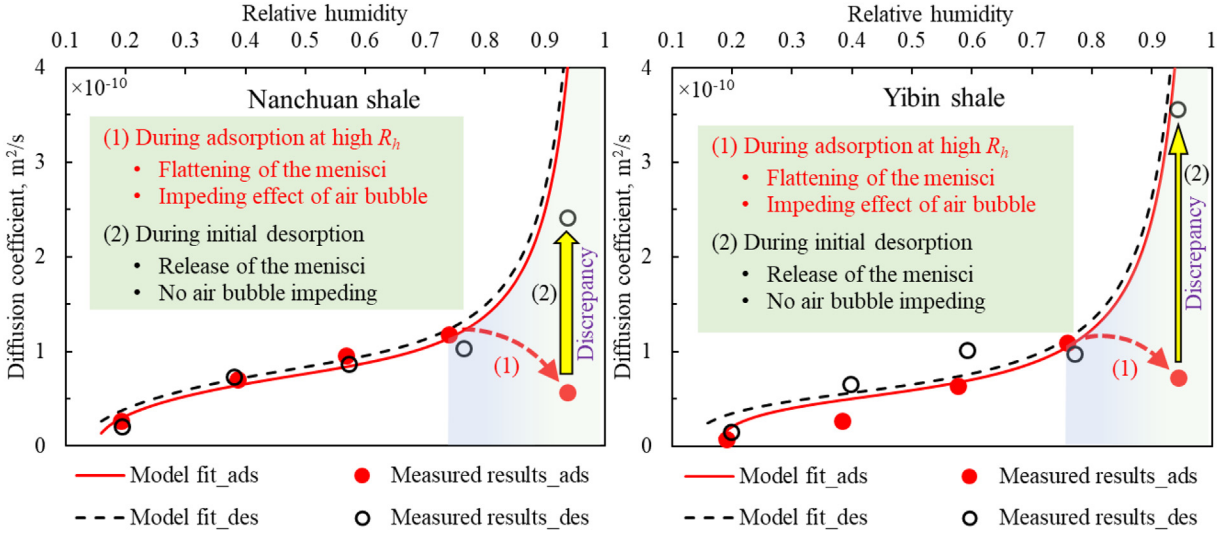

Fig. 7. Comparison between model and observations for Nanchuan (*left*) and Yibin (*right*) shales. Fitting parameters are $\tau_s^* = 16$, $\tau_l^* = 30$, n = 0.5 for Nanchuan shale; and $\tau_s^* = 18$, $\tau_l^* = 30$, n = 0.5 for Yibin shale and are constant with R_h and for both adsorption and desorption.

viscous flux of capillary condensate to the total flux is insignificant compared to that of surface flow of the adsorbed phase at $R_h < 0.96$. Therefore, a reduction in capillary suction pressure may not be the major reason for the reduced diffusion coefficient at high R_h (> 0.8) during adsorption.

Another theory to rationalize the occurrence of a peak in diffusivity at high R_h is that the appearance of capillary condensate will cause the occlusion of narrow pores (Uhlhorn et al., 1992; Yoshimoto et al., 2017) thus increasing the characteristic lengths for transport in the remaining partially-wet network of pores (Yoshimoto et al., 2017). In other words, the occlusion of the narrow pores by capillary condensation increases the tortuosity τ_s for the surface flow of the adsorbed phase, hence reducing the effective permeability of these pores as defined in Eq. (11). However, this theory fails to explain the larger diffusion coefficient at the beginning of the desorption process (Fig. 7) since capillary blockage may also extend the tortuosity and thus impede surface diffusion during initial desorption process.

Based on the above characterizations, feasible diffusion and flow regimes in a single capillary that are consistent with our observations can be possibly codified as in Fig. 9. At low R_h values, water molecules partly adsorb to the pore surfaces as a discontinuous monolayer. Surface diffusion of water molecules within this discontinuous monolayer coverage is driven by the chemical potential gradient and surface concentration per unit surface area (Do and Do, 2001). As R_h increases, mono−/multi-layer adsorption and a water film are formed, resulting in an increase in the liquid mass flux due to an enhanced adsorption concentration per unit surface area. When the R_h increases to a threshold, water clusters/wetting film on opposing pore walls spontaneously connect to form a liquid bridge (Li et al., 2017). Due to the heterogeneity in wettability within any single capillary, an entrapped air bubble may occur (Alratrout et al., 2018), which will impede flow through the capillary (Marchessault and Mason, 1960). With a further increase in relative humidity, the flattening of the meniscus at the pore mouth will cause a further decrease in pore diffusivity due to the loss of capillary forces. At very high R_h, and depending on the pore size, the meniscus and entrapped air bubble will eventually be fully infilled with condensed liquid water. At this stage, viscous flow of the condensed liquid water will conform to the saturated flow in the capillary following the Hagen-Poiseuille equation (Rhim and Hwang, 1975; Lee and Hwang, 1986; Choi et al., 2001). Since the driving force for the viscous flow of the water condensate is the gradient of total gas pressure (zero in this case), the fully-filled capillaries contribute nothing to the total flux.

As desorption begins, pore diffusivity is initially large but declines

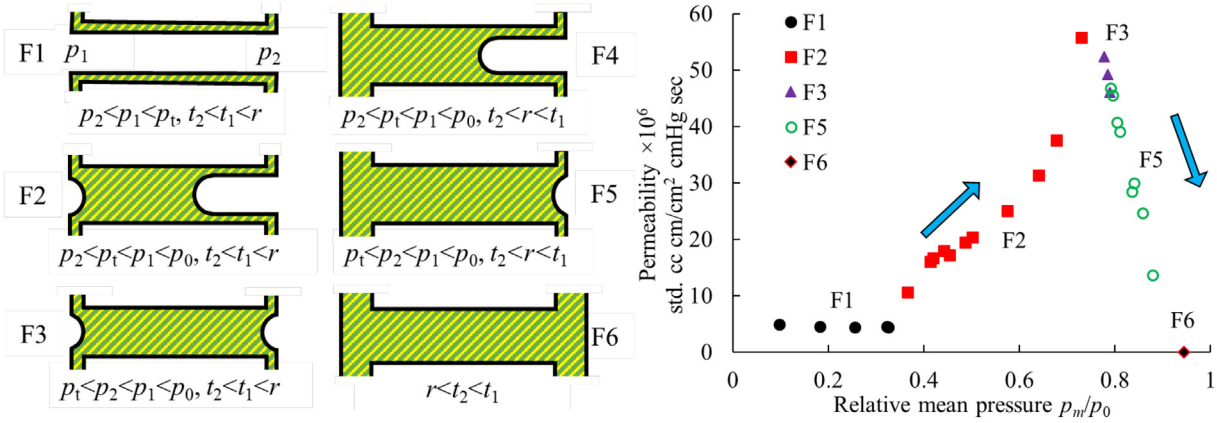

Fig. 8. Six-mode flow model (*left*) and modeled permeability of water vapor through porous Vycor glass as a function of relative mean pressure (*right*) as proposed by Lee and Hwang (1986). p_1, p_2, p_t and p_0 are upstream vapor pressure, downstream vapor pressure, capillary condensation pressure, and saturated vapor pressure, respectively; t_1 and t_2 are adsorption thicknesses; r is the radius of the capillary; F1-F6 are six different flow modes defined on the basis of a single cylindrical capillary.

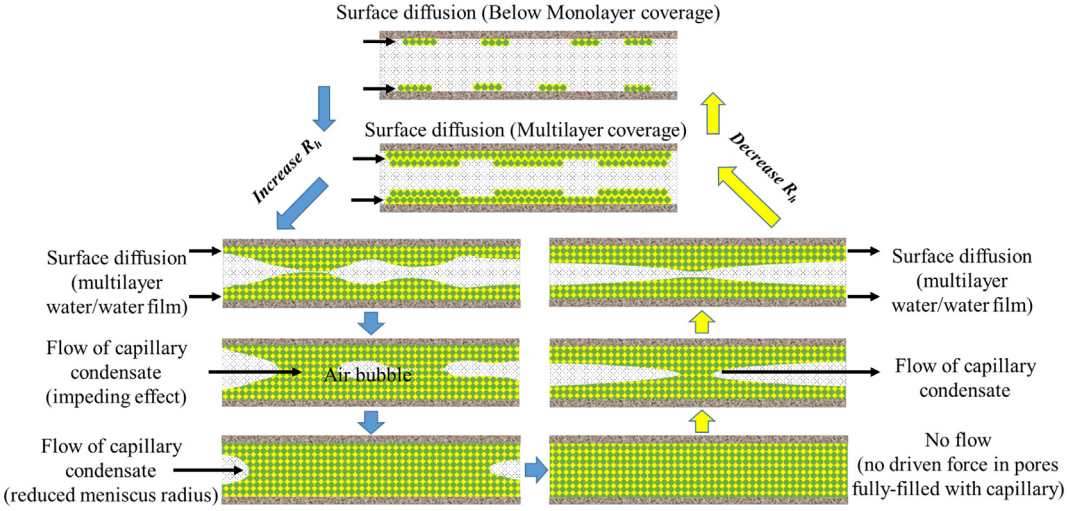

Fig. 9. Schematic of diffusion and flow regimes in a single capillary (after (Do and Do, 2001)). During the adsorption process, the form of the air bubble during capillary condensation may impede the liquid mass flux. Loss of capillary pressure due to a reduction in the radius of the meniscus can also induce a decrease in the mass flux.

as R_h drops (Fig. 7). The higher initial diffusivity results in an obvious discrepancy in diffusivity between the adsorptive and desorptive stages at high R_h (~0.94), resulting possibly from either/both of two reasons. The release of the meniscus results in an increase in the capillary pressure driving the viscous flow of the condensate. Conversely, surface diffusion of the adsorbed phase and the flow of capillary condensate are free from the impeding effect of entrained air bubbles. Following rupture of the capillary bridge as desorption continues, diffusivity declines with the decrease in R_h (Fig. 7) due to the decrease of surface concentration. Since surface flow of the adsorbed phase may co-exist with the viscous flow of the condensate, albeit in capillaries of different radii, the total flux is a summation of each flow mode for each family of pore radii. The roles of different phase types and pore sizes is discussed in the following sections.

4.3. Effect of phase type on sorption and transport

We assume that both adsorbed phase and condensed phase have the same density as liquid water. According to Eqs. (5), (7) and (8), the percentages of the condensed liquid phase, adsorbed phase, and total fraction of water uptake (saturation) in the pores for the Nanchuan shale were calculated on the basis of the pore size distribution characterized by low pressure N_2 adsorption. This estimated total water uptake in the pores defines the saturation and may be independently estimated based from the water vapor adsorption isotherm. Fig. 10 shows an excellent agreement between the modeling result and experimental observations. As R_h increases, the proportion of condensed phase within the pores increases while the proportion of the adsorbed phase remains near constant for $R_h < 0.9$ with a rapid decrease at $R_h > 0.96$. The rapid decrease in the proportion of the adsorbed phase as R_h approaches unity is attributed to the overwhelming dominance of capillary condensation at very high R_h. Fig. 10 also shows that the adsorbed phase dominates the style of water storage at low R_h values (< 0.6) before the condensed phase becomes dominant as $R_h > 0.6$ and becomes the principal/sole storage mode as $R_h > 0.96$. The model provides clarity in the evolution of storage modes with relative humidity – from adsorption dominant al low R_h, transiting to increasing condensation dominant at increasing R_h before becoming condensation only as R_h approaches unity.

Based on the modeling results, the contribution of each flow mode to the total fluid flux may be divided into two components as illustrated in Fig. 11. Surface flow of the adsorbed phase contributes significantly to the total fluid flux over a wide range of R_h values (< 0.96). This is consistent with previous studies that surface diffusion dominates during the transport process of adsorbates in nanoporous media (Schneider and Smith, 1968; Butt and Reed Jr, 1971; Choi et al., 2001; Sirghi, 2012). However, viscous flow of the capillary condensate begins to dominate for $R_h > 0.98$ where capillary condensation is present in the macropores. This extremely high relative humidity, resulting from either a high partial pressure of water vapor or a low saturated pressure of water vapor, would occur in the shale matrix at the beginning of the water production process after several months of the well shut-in period. In this case, viscous flow of capillary water will control the water transport behavior in the shale reservoir. After the drainage of liquid water in the fracture network, the moist gas (shale gas laden with moisture) within the shale matrix will begin to desorb and may be recovered from the well. During this process, the liquid water flux is dominated by surface flow at the lower relative pressure of water vapor as indicated in Fig. 11. Future work on shale gas transport behavior under different partial pressures of water vapor must accommodate such concepts and processes if accurate estimates of gas liberation are to be obtained.

4.4. Effect of pore size on sorption and transport

Based on the scale-based transformation of forces controlling

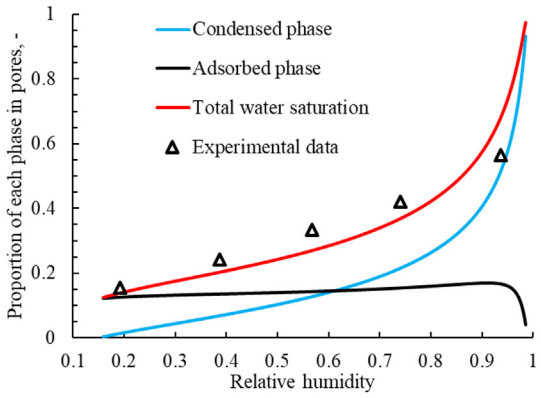

Fig. 10. Proportions of water stored in condensed and adsorbed states as a fraction of total water uptake (saturation) in pores for Nanchuan shale. Experimental data (triangular symbols) refer to the total water uptake in pores estimated by the measured adsorption isotherm.

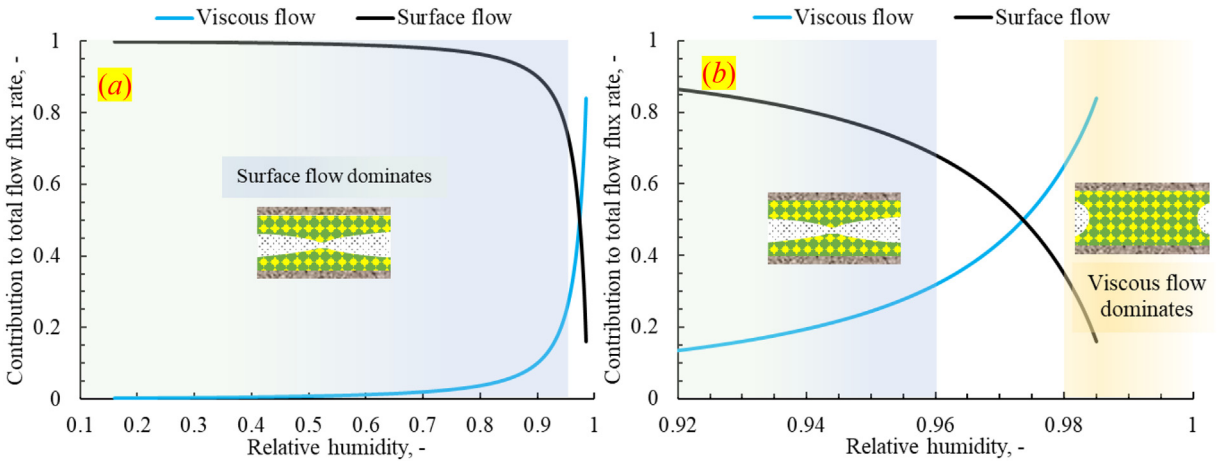

Fig. 11. Contribution of phase types to the total liquid water flux over a spectrum of R_h values for Nanchuan shale: (*a*) R_h ranging from 0.1 to 1; (*b*) R_h ranging from 0.92 to 1.

sorptive behavior, the IUPAC classification divides pores into three size categories according to radius: micropores (< 2 nm), *meso*pores (2–50 nm) and macropores (> 50 nm) (Sing, 1985). The role of pore types (according to the IUPAC classification) in controlling water vapor sorption and transport behavior are discussed in the following.

The relative contributions of the three types of pores to total water sorption under different R_h are shown in Fig. 12, on a mass basis. Mesopores (2–50 nm) contribute most to the total water sorption (56%–81%) over the entire range of relative humidity; the contribution of micropores to the total water sorption decreases with R_h, but remains high (~7%–41%) compared to the contribution of macropores except at $R_h < 0.95$ when macropores become dominant over the micropores. The overwhelmingly dominant contribution of meso−/micro-pores to the total water uptake is due to the dominance of the meso−/micro-pore volume in contributing to the porosity of shales (Sang et al., 2018).

In spite of the significant amount of sorbed water present within the micropores (7%–41% in Fig. 12), the percentage of the water flux carried within the micropores is smaller than 0.5% (Fig. 13). According to Eqs. (11) and (20), the effective/intrinsic permeability of pores correlates positively with pore radius. Regardless of the larger number of micropores, the very small pore size results in a very low intrinsic permeability contributed by the micropores (proportional to r^2 when saturated), and hence results in almost no contribution to the total fluid flux. Besides, despite the insignificant contribution of the macropores (> 50 nm) to the total water uptake (Fig. 12), macropores play an important role in the transport of water vapor in shale. As is shown in Fig. 13. At $R_h < 0.96$, macropores contribute to ~68–78% of the total fluid flux with this decreasing slightly with relative humidity; at $0.96 < R_h < 0.99$, the contribution of the macropores to this flux increases with R_h and asymptotes to ~100% for $R_h > 0.99$, when largest mesopores (50 nm) begin to be fully-filled with capillary condensation. Thus, mesopores have an opposite contribution to the total fluid flux compared to macropores. These phenomena can be explained as follows.

Our proposed transport model divides pores into three different classes at a particular R_h based on a critical pore radius r_{ca} and including a condensed film thickness l_s ($l_s < r_{ca}$). The three categories are for pores with vapor and adsorbed phase (radii > r_{ca}), pores partially filled with capillary water ($l_s <$ radii < r_{ca}) and pores fully filled with condensate (radii < l_s), among which the fully-filled pores have no contribution to the total flux as is indicated by Eq. (20). Fig. 14 shows the different flow modes within the micro−/meso−/macro-pores over the entire range of R_h values based on the appropriate transport model. At $R_h < 0.96$, surface flow dominates in the macropores (Fig. 14 and Fig. 11). The high contribution (~68–78%) of macropores to the total surface flux at $R_h < 0.96$ (Fig. 13) is attributed to the high effective permeability of macropores associated with the adsorbed phase according to Eq. (11). At $R_h > 0.96$, viscous flow of capillary condensation begins within the macropores while a fraction of the mesopores are fully-filled with capillary condensation. This causes an increased contribution of the macropores to total flux with a reduced contribution from the mesopores. At $R_h > 0.99$, even the largest mesopores (50 nm) are fully-filled with capillary condensation according to Fig. 14, leaving no contribution from the mesopores to the total fluid flux due to the lack of capillary forces (Fig. 13). At this stage, the macropores contribute the entire fluid flux until R_h reaches unity (Fig. 13), defining the fully-saturated state of the nano-porous shale.

4.5. Sensitivity of temperature

According to Eq. (26), temperature affects the transport properties in shale pore network in terms of serval parameters including temperature itself (T), dynamic viscosity (μ_s, μ_l), effective/intrinsic permeability of adsorbed (K_s) and condensed phases (K_l), and sorption isotherms ($dm_{w\%}/dR_h$). Assuming the pore structure is independent of temperature, the effect of temperature on effective/intrinsic permeability of adsorbed (K_s) and condensed phases (K_l), and sorption isotherms ($dm_{w\%}/dR_h$) are controlled by the sorption thickness and critical radius for capillary condensation as detailed in section 2. To better

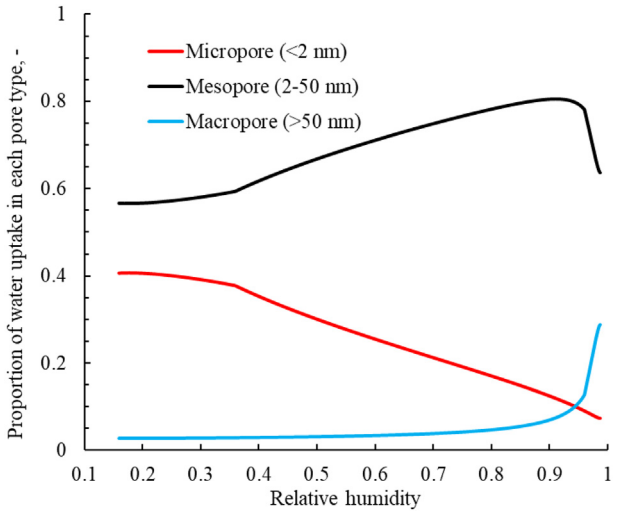

Fig. 12. Proportion of water uptake in micro-, meso-, and macro- pores relative to the total water uptake at different R_h values.

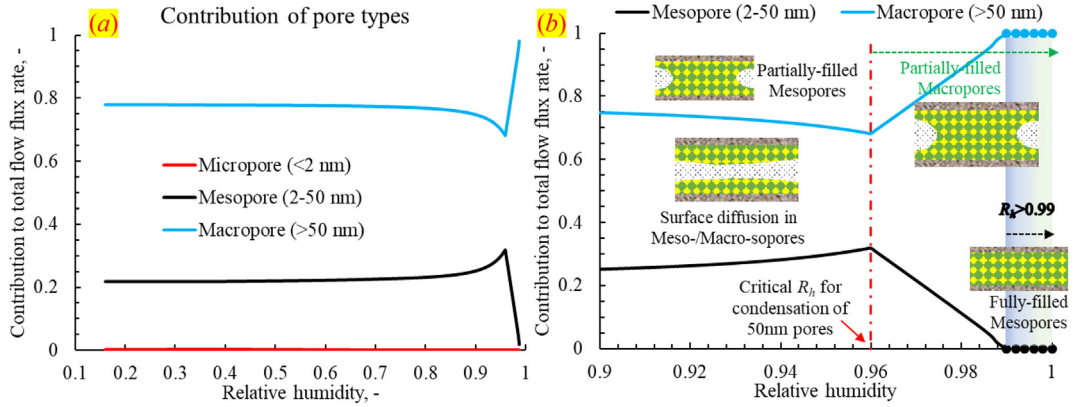

Fig. 13. Contribution of pore types to the total fluid flux over the spectrum of R_h values. (*a*) R_h scale ranges from 0.1 to 1; (*b*) R_h scale ranges from 0.9 to 1.

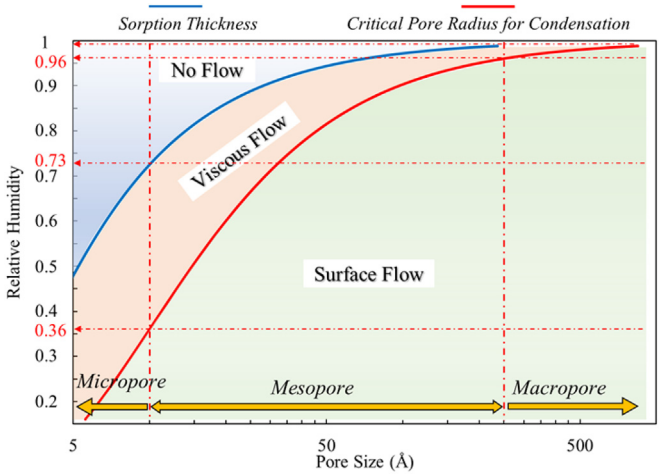

Fig. 14. Different flow modes potentially occurring in micro−/meso−/macro-pores under the spectrum of R_h conditions. Note that pore size refers to the radius of the capillaries. Flow modes occurring in different pore sizes are classified based on a critical pore radius r_{ca} for condensation and film thickness l_s ($l_s < r_{ca}$). Given a pore size r, if $r > r_{ca}$, only surface flow occurs; if $l_s < r < r_{ca}$, only viscous flow of condensate occurs; if $r < l_s$, no flow occurs in this pore.

evaluate our model, we conducted the sensitivity analysis of temperature (from 30 °C to 90 °C) in two scenarios: constant viscosity and temperature-dependent viscosity. For the second scenario, the dynamic viscosity at the four temperatures (30, 50, 70, 90 °C) are listed in Table 4. The results of the two scenarios are shown in Fig. 15 and Fig. 16, respectively.

First, we discuss the first scenario without considering the temperature-dependent viscosity. Fig. 15 shows that temperature tends to have an insignificant effect on the diffusion coefficient of water vapor in terms of surface diffusion of adsorbed phase and viscous flow of condensed phase. Intuitively, high temperature accelerates the water vapor transport and enhances water sorption kinetics as expressed explicitly in Eq. (26). However, temperature also has a negative effect on water uptake (Tang et al., 2017; Sang et al., 2019) in pore network, including sorption on pore surfaces and form of capillary condensation, which in turn influences the transport behavior of water vapor. For example, viscous flow of condensed water slightly decreases as temperature increases as shown in Fig. 15 (*b*), resulting from the smaller intrinsic permeability (K_l) of the condensed phase at higher temperature. Surface diffusion of adsorbed phase (Fig. 15 (*c*)), as influenced by the combined effects of sorption thickness (l_s) and effective permeability (K_s) of the pore network associated with the adsorbed phase, behaves a non-monotonic relation with temperature. Note that we ignore the bulk diffusion of water vapor in the pore network since flow of vapor phase in nano-scale pores can be negligible when compared to the dominant contributions of surface flow and flow of capillary condensate (Schneider and Smith, 1968; Butt and Reed Jr, 1971; Choi et al., 2001; Sirghi, 2012). However, the bulk diffusion of water vapor may be enhanced at high temperature conditions, which may lead to an apparent increase of diffusivity at higher temperatures. Future work is still required to explore the role of bulk diffusion of water vapor at higher temperatures.

In comparison, the effect of temperature on diffusion coefficient of water vapor in the second scenario are shown in Fig. 16, which takes the temperature-dependent viscosity into consideration. It can be observed that diffusion coefficient is apparently enhanced at high temperatures. Compared the results of the two scenarios as shown in Fig. 15 and Fig. 16 respectively, one can infer that higher temperature tends to accelerate water flux through shale pore network due to a lower viscosity (lower viscous resistance). In other words, under higher reservoir temperatures, the drainage/imbibition of water vapor in shale pore systems can be apparently faster than that at lower reservoir temperatures.

5. Summary and conclusion

Mechanisms of water vapor transport in nano-porous shale matrix are explored through an integrated program of experiments and modeling. This defines a proposed model that accommodates both surface diffusion of an adsorbed phase and viscous flow of condensed water – each based on a realistic distribution of measured pore sizes. This pore size distribution is recovered independently from low pressure nitrogen adsorption measurements on two shales. The transport model is validated against measured sorption isotherms and the evolution of diffusion coefficients recovered from dynamic vapor sorption (DVS) experiments. The findings from this study can provide guidance for the shale engineering for shale gas production enhancement by optimized water soaking. Several summary comments and conclusions can be made as follows.

1. Measured diffusion coefficients for water vapor within the shale matrix are of the order of 10^{-12} - 10^{-10} m^2/s. These water vapor sorption isotherms are hysteretic. Higher sorption capacity can be attributed to the higher content of hydrophilic clay minerals and

Table 4
Temperature-dependent dynamic viscosity.

Temperature, °C	30	50	70	90
Dynamic viscosity of liquid water, Pa·s	0.000798	0.000547	0.000402	0.000315

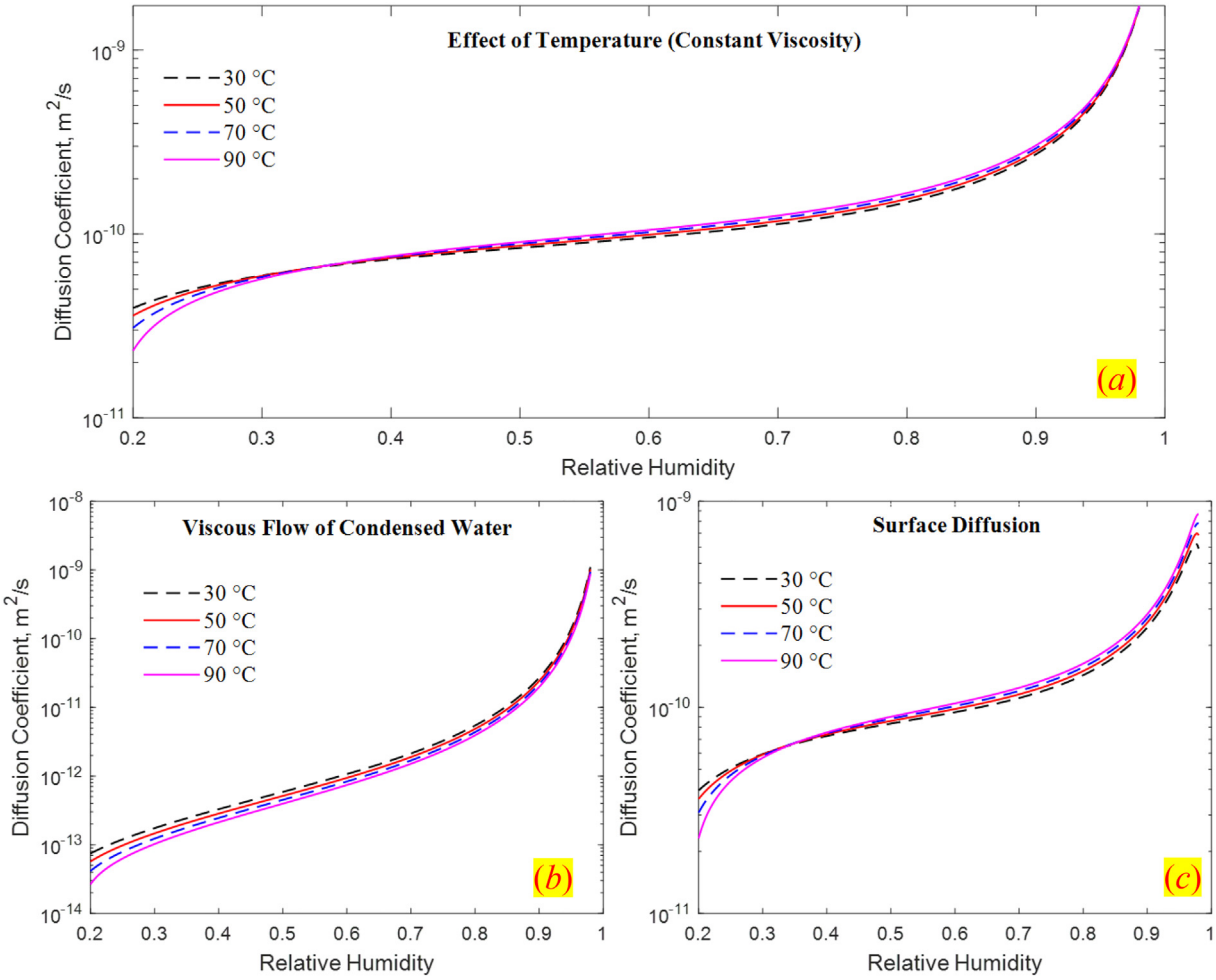

Fig. 15. Sensitivity of temperature on diffusion coefficient of water vapor in shale pores for the scenario of constant viscosity. (*a*) Overall effect of both surface diffusion of adsorbed phase and viscous flow of condensed phase; (*b*) viscous flow of condensed phase; (*c*) surface diffusion of adsorbed phase.

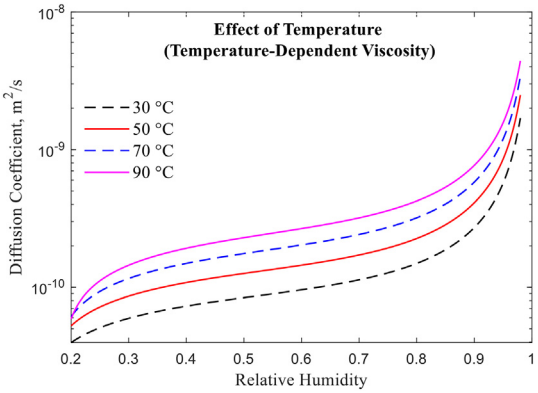

Fig. 16. Sensitivity of temperature on diffusion coefficient of water vapor in shale pores for the scenario of temperature-dependent viscosity.

larger pore volumes present in the contrasting samples.

2. The transport model accurately describes the diffusion behavior of water vapor during the desorption process. The overall diffusion coefficient increases with an increase in R_h since higher R_h corresponds to higher surface concentration gradients. During the adsorption process, however, the drop in diffusion coefficient at high R_h can be attributed to the flattening of the menisci against the pore surface and the impeding effect of entrained air bubbles trapped within the capillary.
3. The model results show that adsorbed water dominates the total water uptake at $R_h < 0.6$ while capillary condensation dominates at $R_h > 0.6$. For transport behavior, surface flow of adsorbed water dominates the total water flux at $R_h < 0.96$ switching to capillary condensation dominant at very high relative humidity ($R_h > 0.98$).
4. Water vapor sorption and transport behavior are both highly dependent on individual pore sizes. Micropores (< 2 nm) contribute to ~7%–41% of the total water uptake over the entire range of relative humidity but play an insignificant role in the transport behavior. Conversely, macropores (> 50 nm) contribute little to the total water adsorption but account for more than 68% of the total flux due to their large intrinsic permeability. The intermediate-sized mesopores play an important role in both water vapor adsorption and transport behaviors within the shale matrix.
5. The diffusion coefficient of water vapor in shale pore network can be enhanced at high reservoir temperatures due to a lower viscous resistance of water to both surface flow and viscous flow.

Declaration of Competing Interest

The authors declare that they have no known competing financial interests or personal relationships that could have appeared to influence the work reported in this paper.

Acknowledgement

This work was financially supported by The U.S. National Institute

of Occupational Safety and Health (NIOSH) under the contract No. NIOSH-200-2016-90385.

References

Alratrout, A., Blunt, M.J., Bijeljic, B., 2018. Wettability in complex porous materials, the mixed-wet state, and its relationship to surface roughness. Proc. Natl. Acad. Sci. 115, 8901–8906.

Bousige, C., Ghimbeu, C.M., Vix-Guterl, C., Pomerantz, A.E., Suleimenova, A., Vaughan, G., Garbarino, G., Feygenson, M., Wildgruber, C., Ulm, F.-J., 2016. Realistic molecular model of kerogen's nanostructure. Nat. Mater. 15, 576–582.

Brattli, B., Broch, E., 1995. Stability problems in water tunnels caused by expandable minerals. Swelling pressure measurements and mineralogical analysis. Eng. Geol. 39, 151–169. https://doi.org/10.1016/0013-7952(95)00009-5.

Butt, J.B., Reed Jr., E.M., 1971. Surface diffusion of single sorbates at low and intermediate surface coverage. J. Phys. Chem. 75, 133–141.

Chen, Y., Yang, R.T., 1998. Surface and mesoporous diffusion with multilayer adsorption. Carbon N. Y. 36, 1525–1537.

Cheng, Y., 2010. Impact of water dynamics in fractures on the performance of hydraulically fractured wells in gas shale reservoirs, in: SPE International Symposium and Exhibition on Formation Damage Control. Society of Petroleum Engineers.

Choi, J.-G., Do, D.D., Do, H.D., 2001. Surface diffusion of adsorbed molecules in porous media: monolayer, multilayer, and capillary condensation regimes. Ind. Eng. Chem. Res. 40, 4005–4031.

Clarkson, C.R., Solano, N., Bustin, R.M., Bustin, A.M.M., Chalmers, G.R.L., He, L., Melnichenko, Y.B., Radliński, A.P., Blach, T.P., 2013. Pore structure characterization of north American shale gas reservoirs using USANS/SANS, gas adsorption, and mercury intrusion. Fuel 103, 606–616.

Cohan, L.H., 1938. Sorption hysteresis and the vapor pressure of concave surfaces. J. Am. Chem. Soc. 60, 433–435.

Crank, J., 1979. The Mathematics of Diffusion. Oxford University Press.

Curtis, J.B., 2002. Fractured shale-gas systems. Am. Assoc. Pet. Geol. Bull. 86, 1921–1938.

Cychosz, K.A., Guillet-Nicolas, R., García-Martínez, J., Thommes, M., 2017. Recent advances in the textural characterization of hierarchically structured nanoporous materials. Chem. Soc. Rev. https://doi.org/10.1039/c6cs00391e.

Do, D.D., 1996. A model for surface diffusion of ethane and propane in activated carbon. Chem. Eng. Sci. 51, 4145–4158.

Do, D.D., 1998. Adsorption Analysis: Equilibria and Kinetics. Imperial College Press, London.

Do, H.D., Do, D.D., 2001. A new diffusion and flow theory for activated carbon from low pressure to capillary condensation range. Chem. Eng. J. 84, 295–308.

Everett, D.H., Haynes, J.M., 1972. Model studies of capillary condensation. I. Cylindrical pore model with zero contact angle. J. Colloid Interface Sci. 38, 125–137.

Fan, L., Ma, L., Yu, Y., Wang, S., Xu, Y., 2019. Water-conserving mining influencing factors identification and weight determination in Northwest China. Int. J. Coal Sci. Technol. 6, 95–101. https://doi.org/10.1007/s40789-018-0233-2.

Fisher, L.R., Gamble, R.A., Middlehurst, J., 1981. The Kelvin equation and the capillary condensation of water. Nature 290, 575.

Flood, E.A., 1961. Adsorption potentials, adsorbent self-potentials and thermodynamic equilibria. Solid surfaces gas-solid interface. Am. Chem. Soc., Washington, Adv. Chem. Ser. 249.

Flood, E.A., Huber, M., 1955. Thermodynamic considerations of surface regions: adsorbate pressures, adsorbate mobility, and surface tension. Can. J. Chem. 33, 203–214.

Flood, E.A., Tomlinson, R.H., Leger, A.E., 1952. The flow of fluids through activated carbon rods: iii. The flow of adsorbed fluids. Can. J. Chem. 30, 389–410.

Gasparik, M., Bertier, P., Gensterblum, Y., Ghanizadeh, A., Krooss, B.M., Littke, R., 2014. Geological controls on the methane storage capacity in organic-rich shales. Int. J. Coal Geol. 123, 34–51.

Gilliland, E.R., Baddour, R.F., Russell, J.L., 1958. Rates of flow through microporous solids. AICHE J. 4, 90–96.

Gregg, S.J., Sing, K.S.W., Salzberg, H.W., 1982. Adsorption, surface area and porosity. J. Electrochem. Soc. 114, 279C.

Holditch, S.A., 1979. Factors affecting water blocking and gas flow from hydraulically fractured gas wells. J. Pet. Technol. 31, 1–515.

Huang, S.L., Aughenbaugh, N.B., Rockaway, J.D., 1986. Swelling pressure studies of shales. Int. J. Rock Mech. Min. Sci. 23, 371–377. https://doi.org/10.1016/0148-9062(86)90005-7.

Israelachvili, J.N., 2011. Intermolecular and Surface Forces. Academic Press.

Jaguste, D.N., Bhatia, S.K., 1995. Combined surface and viscous flow of condensable vapor in porous media. Chem. Eng. Sci. 50, 167–182.

Javadpour, F., Fisher, D., Unsworth, M., 2007. Nanoscale gas flow in shale gas sediments. J. Can. Pet. Technol. 46.

Lahn, L., Bertier, P., Seemann, T., Stanjek, H., 2020. Distribution of sorbed water in the pore network of mudstones assessed from physisorption measurements. Microporous Mesoporous Mater. 295, 109902.

Lee, K.-H., Hwang, S.-T., 1986. The transport of condensible vapors through a microporous vycor glass membrane. J. Colloid Interface Sci. 110, 544–555.

Li, J., Li, X., Wu, K., Feng, D., Zhang, T., Zhang, Y., 2017. Thickness and stability of water film confined inside nanoslits and nanocapillaries of shale and clay. Int. J. Coal Geol. 179, 253–268.

Li, J., Chen, Z., Wu, K., Li, R., Xu, J., Liu, Q., Qu, S., Li, X., 2018a. Effect of water saturation on gas slippage in tight rocks. Fuel 225, 519–532.

Li, R., Wu, K., Li, J., Xu, J., Chen, Z., 2018b. Gas transport in shale nanopores with mobile high-viscosity water film. Ind. Eng. Chem. Res. 57, 11219–11228.

Luzar, A., Chandler, D., 1996. Hydrogen-bond kinetics in liquid water. Nature 379, 55.

Marchessault, R.N., Mason, S.G., 1960. Flow of entrapped bubbles through a capillary. Ind. Eng. Chem. 52, 79–84.

Naumov, S., Valiullin, R., Galvosas, P., Kärger, J., Monson, P.A., 2007. Diffusion hysteresis in mesoporous materials. Eur. Phys. J. Spec. Top. 141, 107–112.

Okazaki, M., Tamon, H., Toei, R., 1981. Interpretation of surface flow phenomenon of adsorbed gases by hopping model. AICHE J. 27, 262–270.

Pang, Y., Wang, G., Ding, Z., 2014. Mechanical model of water inrush from coal seam floor based on triaxial seepage experiments. Int. J. Coal Sci. Technol. 1, 428–433. https://doi.org/10.1007/s40789-014-0049-7.

Ravikovitch, P.I., Neimark, A.V., 2005. Diffusion-controlled hysteresis. Adsorption 11, 265–270.

Raviv, U., Laurat, P., Klein, J., 2001. Fluidity of water confined to subnanometre films. Nature 413, 51–54.

Rhim, H., Hwang, S.-T., 1975. Transport of capillary condensate. J. Colloid Interface Sci. 52, 174–181.

Rouquerol, J., Rouquerol, F., Llewellyn, P., Maurin, G., Sing, K.S.W., 2013. Adsorption by Powders and Porous Solids: Principles, Methodology and Applications. Academic Press.

Rowell, R.L., Carrano, S.A., De Bethune, A.J., Malinauskas, A.P., 1971. Gas and vapor permeability: Surface flow through porous media. J. Colloid Interface Sci. 37, 242–246.

Sang, G., Elsworth, D., Miao, X., Mao, X., Wang, J., 2016. Numerical study of a stress dependent triple porosity model for shale gas reservoirs accommodating gas diffusion in kerogen. J. Nat. Gas Sci. Eng. 32, 423–438. https://doi.org/10.1016/j.jngse.2016.04.044.

Sang, G., Liu, S., Zhang, R., Elsworth, D., He, L., 2018. Nanopore characterization of mine roof shales by SANS, nitrogen adsorption, and mercury intrusion: Impact on water adsorption/retention behavior. Int. J. Coal Geol. 200, 173–185. https://doi.org/10.1016/j.coal.2018.11.009.

Sang, G., Liu, S., Elsworth, D., 2019. Water vapor sorption properties of Illinois shales under dynamic water vapor conditions: experimentation and modeling. Water Resour. Res. 55, 7212–7228. https://doi.org/10.1029/2019WR024992.

Schneider, P., Smith, J.M., 1968. Chromatographic study of surface diffusion. AICHE J. 14, 886–895.

Seemann, T., Bertier, P., Krooss, B.M., Stanjek, H., 2017. Water vapour sorption on mudrocks. Geol. Soc. London, Spec. Publ. 454, 201–233.

Sing, K.S.W., 1985. Reporting physisorption data for gas/solid systems with special reference to the determination of surface area and porosity (recommendations 1984). Pure Appl. Chem. 57, 603–619.

Sirghi, L., 2012. Transport mechanisms in capillary condensation of water at a single-asperity nanoscopic contact. Langmuir 28, 2558–2566.

Sposito, G., Skipper, N.T., Sutton, R., Park, S., Soper, A.K., Greathouse, J.A., 1999. Surface geochemistry of the clay minerals. Proc. Natl. Acad. Sci. 96, 3358–3364.

Sun, Z., Li, X., Shi, J., Zhang, T., Sun, F., 2017. Apparent permeability model for real gas transport through shale gas reservoirs considering water distribution characteristic. Int. J. Heat Mass Transf. 115, 1008–1019.

Sun, Z., Shi, J., Wu, K., Li, X., 2018. Gas flow behavior through inorganic nanopores in shale considering confinement effect and moisture content. Ind. Eng. Chem. Res. 57, 3430–3440.

Tamon, H., Okazaki, M., Toei, R., 1981. Flow mechanism of adsorbate through porous media in presence of capillary condensation. AICHE J. 27, 271–277.

Tang, X., Ripepi, N., Valentine, K.A., Keles, C., Long, T., Gonciaruk, A., 2017. Water vapor sorption on marcellus shale: measurement, modeling and thermodynamic analysis. Fuel 209, 606–614.

Thommes, M., 2010. Physical adsorption characterization of nanoporous materials. Chem. Ing. Tech. 82, 1059–1073. https://doi.org/10.1002/cite.201000064.

Thommes, M., Morell, J., Cychosz, K.A., Fröba, M., 2013. Combining nitrogen, argon, and water adsorption for advanced characterization of ordered mesoporous carbons (CMKs) and periodic mesoporous organosilicas (PMOs). Langmuir 29, 14893–14902.

Uhlhorn, R.J.R., Keizer, K., Burggraaf, A.J., 1992. Gas transport and separation with ceramic membranes. Part I. Multilayer diffusion and capillary condensation. J. Memb. Sci. 66, 259–269.

Wu, K., Chen, Z., Li, J., Li, X., Xu, J., Dong, X., 2017. Wettability effect on nanoconfined water flow. Proc. Natl. Acad. Sci. 114, 3358–3363.

Yoro, K.O., Amosa, M.K., Sekoai, P.T., Daramola, M.O., 2019. Modelling and experimental investigation of effects of moisture and operating parameters during the adsorption of CO2 onto polyaspartamide. Int. J. Coal Sci. Technol. 6, 225–234. https://doi.org/10.1007/s40789-018-0224-3.

Yoshimoto, Y., Hori, T., Kinefuchi, I., Takagi, S., 2017. Effect of capillary condensation on gas transport properties in porous media. Phys. Rev. E 96, 43112.

Yuan, W., Pan, Z., Li, X., Yang, Y., Zhao, C., Connell, L.D., Li, S., He, J., 2014. Experimental study and modelling of methane adsorption and diffusion in shale. Fuel 117, 509–519.

Zhuravlev, Y.N., Porokhnov, A.N., 2019. Computer simulation of coal organic mass structure and its sorption properties. Int. J. Coal Sci. Technol. 6, 438–444. https://doi.org/10.1007/s40789-019-0256-3.

Zolfaghari, A., Dehghanpour, H., Holyk, J., 2017a. Water sorption behaviour of gas shales: I. Role of clays. Int. J. Coal Geol. 179, 130–138.

Zolfaghari, A., Dehghanpour, H., Xu, M., 2017b. Water sorption behaviour of gas shales: II. Pore size distribution. Int. J. Coal Geol. 179, 187–195.